Room-temperature Facile Synthesis of Co$_3$O$_4$ Nanoflakes as Anode Material for Li-ion Rechargeable Batteries

Venugopal Nulu, Arunakumari Nulu and Keun Yong Sohn[*]

Department of Nanoscience and Engineering, Center for Nano Manufacturing, Inje University
197 Inje-ro, Gimhae, Gyeongnam-do 50834, Republic of Korea
[*]E-mail: ksohn@inje.ac.kr; ksohnlab@gmail.com

There have been numerous reports on the synthesis of Co$_3$O$_4$ nanoparticles with a wide variety of nanostructures using different chemical methods. Many such approaches involved the synthesis of the metal hydroxide followed by thermal annealing to obtain the oxide. Recently, several low-temperature chemical methods have been developed. However, these procedures typically involve tedious experimental parameters. In this study, we developed a simple, strategic room-temperature approach to obtain hierarchical arrays of Co$_3$O$_4$ nanoflakes. The properties of the obtained material (phase, morphology, and structure) were analyzed comprehensively by techniques. The Co$_3$O$_4$ nanoflakes show superior electrode performance as an anode material in Li-ion rechargeable batteries, in terms of cycle life and rate capability, that is suitable for next-generation energy storage applications.

Keywords: room-temperature synthesis; Co$_3$O$_4$ nanoflakes; lithium-ion rechargeable battery; specific capacity

1. INTRODUCTION

Transition metal oxides (e.g., Fe$_3$O$_4$, Fe$_2$O$_3$, CoO, Co$_3$O$_4$, MnO, and Mn$_3$O$_4$) with a wide variety of nanostructures like nanorods, nanoparticles, nanodisks, and nanotubes have been recognized as fascinating materials for energy storage and conversion, catalysis, biotechnology, and sensing [1–4]. Notably, these metal oxides are widely studied as promising high-capacity conversion electrode materials for Li-ion rechargeable batteries (LIBs), and display significantly larger reversible capacities than the commercially used graphite anode material [5–9]. Regrettably, these high-capacity anode electrode materials suffer from the drawbacks of rapid capacity fading and pulverization upon repeated cycling caused by the significant volume change occurring during Li$^+$ ion conversion reactions [6–9]. A common and efficient approach to improve the performance of an electrode material is to design and

synthesize nanostructured electrode materials with different morphologies such as hollow, mesoporous nanorods, nanowires, nanoflakes, and nanosheets. Hierarchically structured nanoflakes, which not only provide increased active surface/interface of materials but also decrease the Li-ion diffusion length owing to the presence of nanometer-thick flakes, are promising for application as electrode materials. Therefore, it is worthwhile to develop simple, large-scale synthetic strategies to obtain new nanostructures of transition metal oxides. Co_3O_4 is one of the promising and extensively studied materials for use as an anode material in LIBs owing to its high theoretical specific capacity, which is much larger than that of the conventionally used graphite anode material [10–12]. However, Co_3O_4 as an anode material undergoes pulverization due to expansion/contraction during the electrochemical conversion reaction with Li, resulting in a substantial, irreversible capacity loss and poor cycle life owing to its low conductivity, significant volume changes, and particle aggregation [8]. In addressing these problems, the preparation of Co_3O_4 nanostructures is of prime importance because their large active surface area increases the activity and they present superior and exceptional properties compared to those of bulk materials. Until now, many accessible and general routes have been developed for the preparation of Co_3O_4 nanostructures with controllable structures on a large scale [13–15]. To this end, various synthetic methods and strategies have been developed, including thermal decomposition of cobalt precursors [16], hydrothermal/ solvothermal methods, chemical vapor deposition [17], chemical spray pyrolysis [18], soft-chemical growth routes, and the traditional sol-gel methods [19]. However, all of these methods require certain harsh conditions, relatively high-temperatures, long reaction times, and specialized equipment such as heating furnaces and autoclaves. In addition, these synthetic methods are also limited by issues such as low product yields and reproducibility.

By contrast, low-temperature or room-temperature methods ensure facile and low-cost processing with the requirement for standard laboratory glassware only. Only a few studies have described the low-temperature synthesis of Co_3O_4 particles (nano- and micron-sized) [20, 21] or nanosheets [22] and their room-temperature synthesis [23]. These methods present drawbacks related to low product yield, reproducibility in terms of structure fabrication, need for the removal of organic template, or the use of expensive ionic liquids as solvents. Overall, it is more appropriate to design a low-temperature, or indeed room-temperature synthetic route to obtain a high yield of the desired Co_3O_4 with a wide variety of structures.

In this work, we describe a simple approach for the synthesis of self-assembled nanoflake arrays of Co_3O_4 using Li_2O_2 as an oxidizing/precipitating agent in an organic solvent at room temperature. This method involves a simple template-free, non-aqueous process performed using simple laboratory glassware. A simple washing of the reaction product, followed by room temperature air-drying, results in the evolution of the Co_3O_4 phase.

2. EXPERIMENTAL

2.1 Material Synthesis

Co_3O_4 nanoflakes were prepared following a previously published procedure with some modifications [24]. After dissolving $Co(NO_3)_2 \cdot 6H_2O$ in 100 mL of ethanol to obtain 0.07 M solution,

0.6 g of Li_2O_2 was added to the solution with vigorous stirring at room temperature in a glass beaker closed with a glass plate. A brown precipitate was formed immediately, which turned black after 1 h. After maintaining the solution overnight under ambient conditions, the precipitate formed was centrifuged and washed repeatedly with deionized (DI) water and ethanol. The precipitate was dried at room temperature for 24 h and its structure, phase, and morphology were characterized. To investigate the reaction mechanism, samples were collected after 1, 2, and 3 h (this sample only was washed with water and ethanol) during the course of the reaction, and the respective air-dried samples were analyzed by X-ray diffraction (XRD).

2.2 Material Characterization

The morphology and microstructure of the obtained material was identified by scanning electron microscopy (SEM, JSM7000F) and transmission electron microscopy (HR-TEM, JEM-2100F). The crystalline structure of the material was examined by powder XRD using Cu-$K\alpha_1$ radiation ($\lambda = 1.54056$ Å) in the range of $10° < 2\theta < 80°$.

2.3 Electrochemical measurements

Electrochemical properties of the Co_3O_4 nanoflakes were evaluated using CR2032 coin cells. The electrode was prepared by mixing the active material, a conductive agent (Ketjen Black), and polyamide imide (PAI) dissolved in *N*-methyl pyrrolidone (NMP) in the ratio of 75:15:10, and coating the slurry on a Cu foil. Subsequently, the coated foil was initially dried at 80 °C for 3 h and then heated in vacuum at 200 °C for 3 h in an oven. The coin-type half-cell was assembled with 1 M $LiPF_6$ ethylene carbonate and dimethyl carbonate (EC/DMC) (1:1) as the electrolyte, Celgard 2300 membrane as the separator, and lithium foil as the counter electrode. Charge/discharge experiments were carried out at different current densities with a cut off voltage of 0.01–3.0 V vs. Li^+/Li at ambient conditions. Cyclic voltammetry was performed with a cutoff voltage of 3 V and scan rate of 3 mV s^{-1}.

3. RESULTS AND DISCUSSION

Fig. 1a displays the XRD pattern of the as-prepared Co_3O_4 nanoflakes. The broad, low-intensity peaks indicate the presence of nano-sized particles. All the reflection peaks could be accurately indexed to purely cubic phase of Co_3O_4 (space group, *Fd3m*; JCPDS No. 42-1467) with a lattice constant of 8.080 Å. No other impurity peaks are detected in the XRD pattern, confirming thus the high purity of the final product prepared at room temperature. To understand the reaction pathway, we also collected samples during the reaction after 1, 2, and 3 h of the reaction. The samples obtained after 1 and 2 h were air dried at room temperature whereas the sample collected after 3 h was washed with water and ethanol before air-drying.
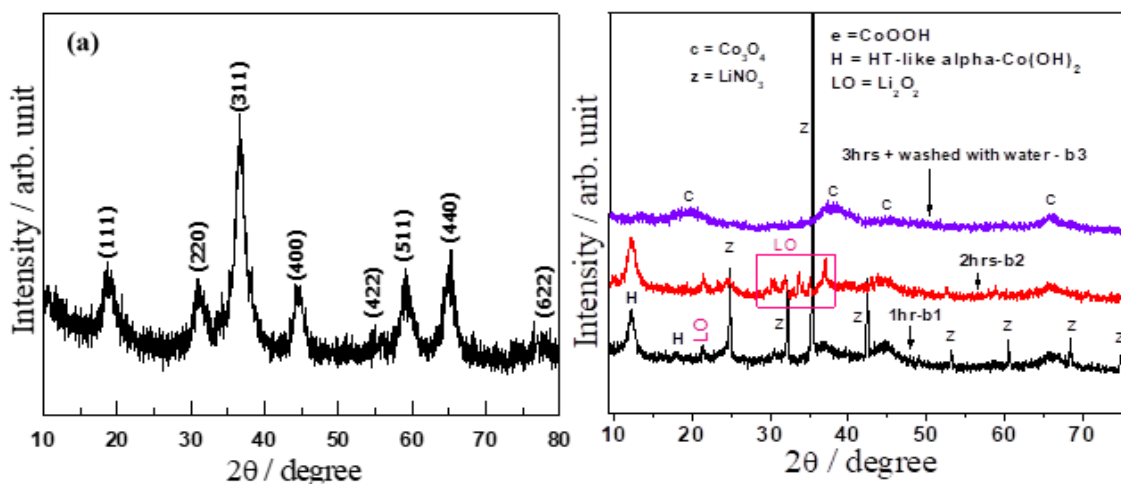
Figure 1. XRD patterns of (a) as-synthesized Co_3O_4 nanoflakes and (b) b1 and b2, which are air-dried solid precipitates collected during the course of the reaction after 1 and 2 h period, respectively. (b) b3 is the sample collected after 3 h of reaction and washed with water and ethanol before drying in air.

Fig. 1b shows the XRD patterns of the products obtained after 1 h (Fig. 1b, b1), 2 h (Fig. 1b, b2), and 3 h (Fig. 1b, b3). The XRD patterns shown in Fig. 1b for b1 and b2 are assigned to a mixture consisting of $LiNO_3$ (marked as *z*, JCPDS 08-0466), Co_3O_4 (marked as *x*, JCPDS 42-1467), untreated Li_2O_2 (marked as LO), and an hydrotalcite (HTlc)-like layered phase ($Co^{II}_{1-x} Co^{III}_x (OH)_2(NO_3)_x \cdot nH_2O$, $d_{003} \geq 7.20$; $d_{003} = 2d_{006} = 3d_{009}$, HTlc Co(II, III)) [24, 25]. These products are obtained by the neutralization of the reaction mixture as a result of the reaction between mildly basic Li_2O_2 and acidic NO_3^- groups of the cobalt nitrate hexahydrate precursor in the non-aqueous ethanol solvent. As a result, $LiNO_3$ salt is formed as one of the primary products with the release of oxygen, which is subsequently used for the oxidation of the Co(II) cations.

As the reaction proceeds further, the residual nitrate ions slowly react with Li_2O_2, resulting in the formation of an oxidative atmosphere. Major peaks related to $LiNO_3$ are not observed in the XRD pattern of the sample obtained after 2 h because the powder collected at this stage was slightly free from the ethanol-soluble $LiNO_3$ salt. Moreover, the Li_2O_2 peaks appeared in the 2 h reaction product ($2\theta = 21.3º$ and between 30–40º, see Fig. 1b, b2), as supported by the presence of a white colored powder in the as-obtained powder. The growth of XRD peaks at the 2θ values of 45º (400) and 67º (440) after 1 h of reaction suggests that the released oxygen might be used in the oxidation of Co(II) ions to Co_3O_4, possibly at the initial stage of the chemical reaction. As the reaction proceeds, initially, there is sustained release of oxygen during the reaction in the closed beaker. The trapped amount of oxygen gas within the covered beaker favors the oxidation of Co(II) to HTlc Co (II, III) hydroxide and subsequently to Co (II, III)$_3O_4$, but not to fully oxidized Co(III). As ethanol acts both as a acidic and a mild reducing agent, the pH of the reaction mixture after 3 h was noted to be 5.8. It has been previously reported that under weak acidic aqueous conditions, Co^{2+} is more prone to be oxidized in the presence of oxygen to form Co_3O_4 [26], and it has also been stated that upon increasing the reaction temperature to 60–90 ºC, Co_3O_4 is eventually produced from the HTlc Co (II, III) hydroxide

intermediate phase. We assume a similar mechanism in our non-aqueous system. Further, $LiNO_3$ and Li_2O_2 salts are easily washed away with water as these products are water-soluble (Li_2O_2 rapidly reacts with water molecules resulting in the formation of oxidizing agents such as H_2O_2 or O_2). During washing with water, the limited amount of unreacted Li_2O_2 present in the sample (sample collected after 3 h) produces oxygen which aids in oxidizing the remaining HTlc Co (II, III) hydroxide in the respective sample to yield the stable Co_3O_4 and leaves a minor quantity of the HTlc phase (see Fig. 1b, b3). Furthermore, allowing the reaction to proceed overnight under ambient conditions followed by washing with double distilled water and ethanol resulted in a completely pure spinel phase with broad XRD peaks of enhanced intensities, as shown in Fig. 1a. Fig. 2 exhibits the typical morphology of Co_3O_4 nanostructures synthesized at room temperature. Apparently, the as-prepared structures are comprised of self-organized, interconnected hierarchical nanoflakes, in which each nanoflake consists of a nanowall with an average diameter of ~6–8 nm, as observed in the SEM image (Fig. 2a). The dark light contrast of the nanoflakes in the TEM image defines ultra-thin wall texture (edge boundaries) of the respective nanoflakes (displayed in Fig. 2b). The high-resolution TEM (HRTEM) image (inset of Fig. 2b) supports the ultrathin feature of the two adjacent nanoflakes.
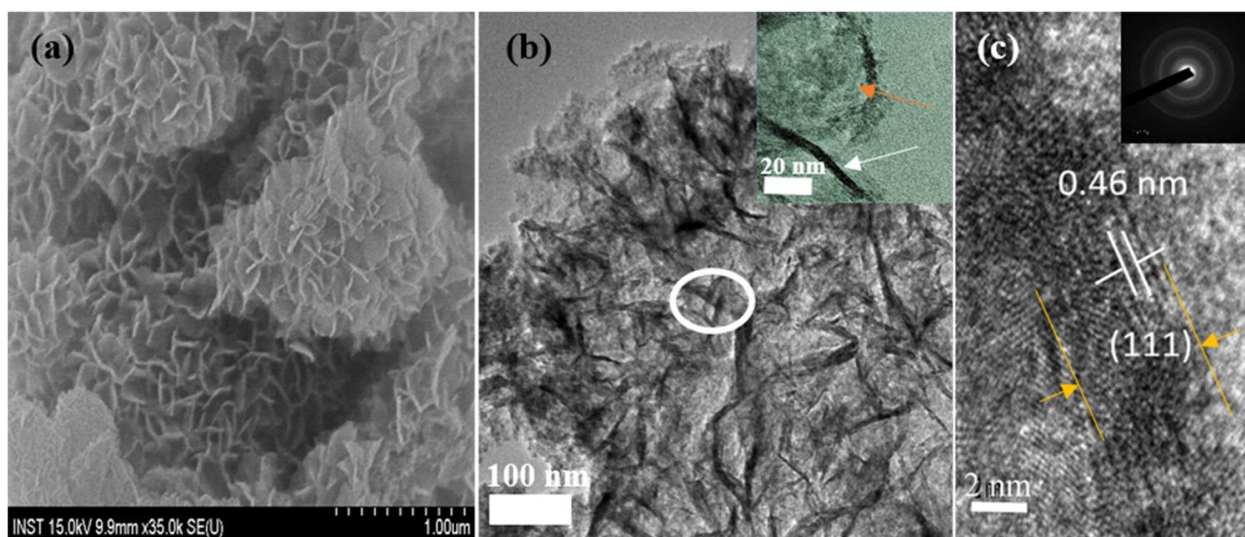

Figure 2. (a) SEM, (b) TEM, and (c) HRTEM images of Co_3O_4 nanoflakes. The inset image in (c) shows two specific nanoflakes marked by arrows. (d) Specific line profile of the ultra-thin nanowall with the (111) facets exposed and the inset shows the selected area electron diffraction pattern obtained for the region marked by a circle in image (b).

Among those nanoflakes shown in TEM image, the one at the bottom exhibits a cross-sectional wall thickness of ~5–8 nm (marked by a white arrow), whereas the side-view of the adjacent nanoflake wall indicates that it is composed of uneven ultrathin amorphous structures together with a mesoporous texture (the region marked with a colored arrow). The corresponding HRTEM image obtained on the flat wall boundary of a specific nanoflake (Fig. 2c) reveals the resolved lattice fringes with *d* values of 0.462 nm, consistent with the value of (111) plane of the Co_3O_4 cubic phase. Notably, most of these

Co_3O_4 nanoflakes dominantly exposed (111) planes as the external surface. The Co_3O_4 phase can be further confirmed by the ring-shaped patterns in the electron diffraction shown in the inset of Fig. 2c.
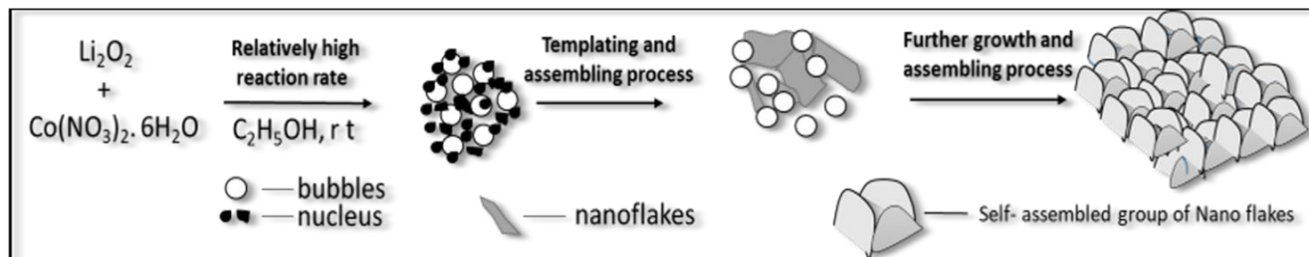
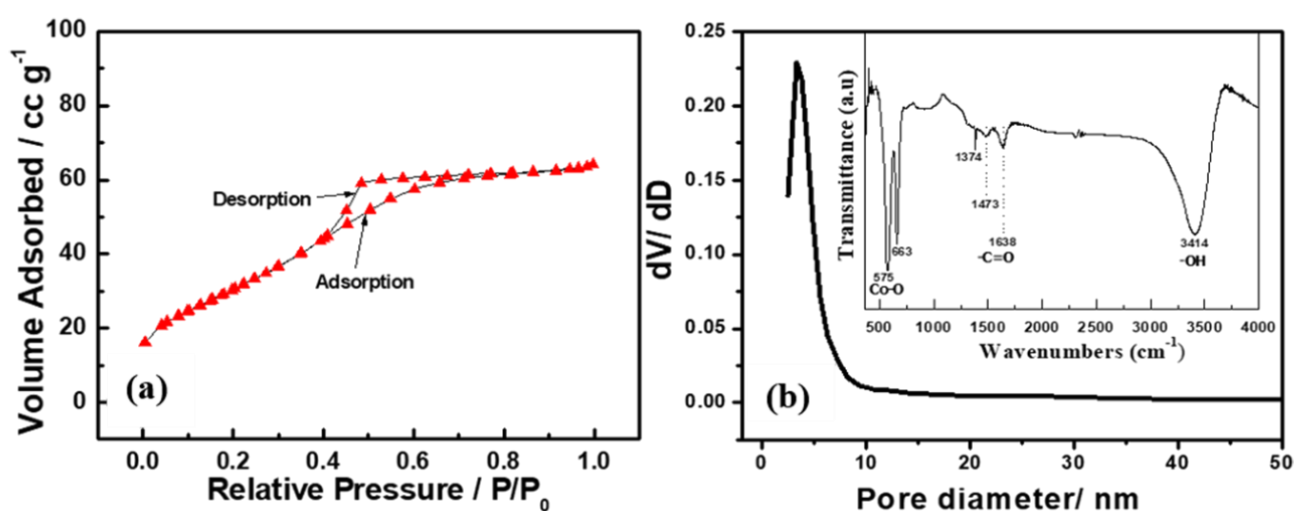**Scheme 1.** Plausible mechanism for the formation of hierarchically organized Co_3O_4 nanoflakes.

Figure 3. (a) N_2 adsorption–desorption isotherms and (b) pore size distribution curves of the Co_3O_4 nanoflakes; inset shows the FTIR spectrum of the sample.

In general, nanoflakes with porous structures are characterized by a large active surface area. The as-prepared Co_3O_4 nanoflakes were characterized by nitrogen adsorption and desorption isotherms at 77.2 K. As shown in Fig. 3a, the adsorption–desorption curves exhibit a typical type IV isotherm with a hysteresis H_2 loop, indicating that the sample has a mesoporous structure ($P/P_0 > 0.4$) with a small number of micro/nanopores; the slit-like pores are obtained from the uneven arrangement of flakes-like structures. The Brunauer−Emmett−Teller (BET) analysis yields a high surface area of ~105.2 m^2 g^{-1} with a pore size distribution curve peaked at ~3–8 nm (Fig. 3b). This result is consistent with the TEM analysis discussed above. The inset shows the FTIR spectrum of the as-synthesized Co_3O_4 nanoflakes, which exhibited strong absorption bands at 575 and 663 cm^{-1}, which are associated with the Co–O stretching vibrations of Co_3O_4 [27]. The O–H stretching and bending vibrations are detected at 3414 cm^{-1}, suggesting the presence of absorbed solvent molecules in the solid matrix; the additional absorption bands at 1638, 1473, and 1374 cm^{-1} are attributed to the –C=O, and –C-O groups of organic compounds, possibly associated with the compounds formed by the oxidation of the solvent and then adsorbed onto the solid precipitate.

Based on the present results and our experimental conditions, a plausible mechanism involving bubble templating coupled with nanoflake self-assembly can be proposed. In our method, Li_2O_2 functions not only as an oxidant but also as a source of O_2 bubbles. Typically, a gas bubbling method is employed to generate hollow structures of different materials.
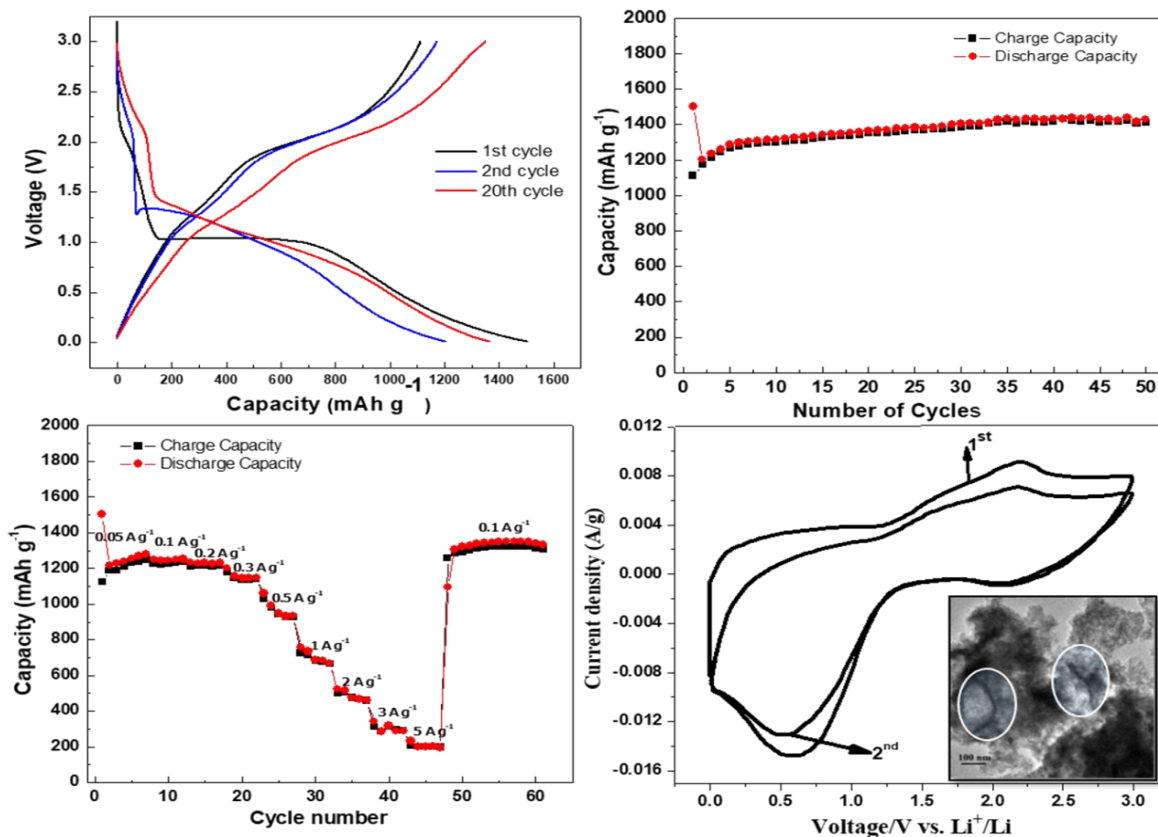

Figure 4. Electrochemical performance of the Co_3O_4 nanoflake material electrode: (a) charge–discharge profiles, (b) cycling stability for 50 cycles, (c) rate performance at different current densities, and (d) CV profiles showing the first two cycles between 3 V and 1 mV at a scan rate of 3 mV s^{-1}.

Indeed, a low reaction rate favors hollow particles whereas a high reaction rate leads to irregular nanostructures [25, 26]. As shown in Scheme 1, initially, amorphous HTlc Co(OH)$_2$ nuclei are formed rapidly through the reaction of Li_2O_2 with cobalt nitrate hexahydrate in ethanol as discussed in the above section at a high reaction rate. Consequently, at the initial stage of the reaction, a particular concentration of O_2 microbubbles was observed to be generated; simultaneously, a high local concentration of the obtained HTlc Co(OH)$_2$ nuclei that diffuse to the gas–liquid interface between the O_2 bubbles and liquid solvent. Moreover, the highly polar solvent molecules adsorb on the freshly formed nuclei, which tend to get enriched at the solid–liquid interface; subsequently, under the continuous course of reaction in the solution during the growth process, the HTlc Co(OH)$_2$ nuclei grow into irregularly shaped nanoflakes. Thus, driven by energy minimization and the limited concentration of oxygen bubbles after a certain reaction period, these nanoflakes self-assemble in a random manner to form bundles. Finally, further growth leads to the formation of longer aggregated structures with the outcome of large structures of hierarchically organized Co_3O_4 nanoflakes. Further, the high polarity of

ethanol plays a crucial role in the course of the crystallization of the mismatched flakes with their (111) planes exposed.

The utility of Co_3O_4 nanoflakes as anode electrodes in Li-ion secondary batteries was investigated by galvanostatic charge–discharge cycling at a current density of 100 mA g^{-1}. Fig. 4a shows the qualitatively very similar charge–discharge profiles (for the 1st, 2nd, and 20th cycle) of the Co_3O_4 nanoflake electrode. In the first potential discharge curve, two noticeable sloping potentials are observed, which are attributed to the irreversible reaction of Co_3O_4 with lithium-ion leading to the formation of a solid electrolyte interphase (SEI) film, which can result in irreversible capacity loss [28]. Two central potential plateaus at 1.26 to 1.23 V are observed in the following discharge curves, corresponding to the Co^{3+}/Co^{2+} and Co^{2+}/Co reduction reactions [29]. As shown in Fig. 4b, the discharge capacities of the Co_3O_4 nanoflake electrode for the 1st, 2nd, 3rd, and 50th cycles are observed to be 1497, 1202, 1237, and 1430 mAh g^{-1}, respectively. The initial low coulomb efficiency (74%) could have resulted from the irreversible Li$^+$ ion conversion reaction caused by the formation of the SEI; however, this value is higher than those reported for different Co_3O_4 nanostructures [24, 28b, 29–31], and the observed efficiency is ~97–98% between 5–50 cycles. After 50 cycles, our nanoflake electrode retains at 95% of the first discharge capacity. All of these capacities are higher than the theoretical capacity of bulk Co_3O_4 (890 mAh g^{-1}). There are several reports on such values that exceed the theoretical capacity that originate from the extra Li$^+$ stored in the pores, SEI films, and nanotextural arrangement of the nanoflakes on the outer surface, all of which provide increased active sites for Li$^+$ ion interaction [24, 30–32]. A performance comparison of Co_3O_4 nanoflakes with other forms of Co_3O_4 and Co_3O_4 composite nanostructures reported to date is provided in Table 1.

Table 1. Electrochemical performance comparison of different forms Co_3O_4 and Co_3O_4 composite nanostructures.

Co_3O_4 nanostructures	Current density (mA g^{-1})	1st discharge capacity (mAh g^{-1})	Capacity upon cycling (mAh g^{-1})	References
Co_3O_4 nanoflakes	100	1497	1437 after 50 cycles	This work
Co_3O_4 and Co_3O_4/carbon nanotubes composite	50	1283 and 1420	398 and 1410 after 50 cycles	24
Co_3O_4@graphene composites	50	1298	740 after 60 cycles	28b
Co_3O_4 nanoparticles; Co_3O_4@graphene film	50	1148, 1350	200; 1120	29
3D hierarchical Co_3O_4 microspheres	200	1310	1228 after 160 cycles	30

Fig. 4c shows the rate performance of the Co_3O_4 nanoflake electrode at various current densities. The results indicate that the Co_3O_4 nanoflake electrode demonstrates an excellent rate performance, exhibiting a good reversible capacity of 1214 mAh g^{-1} at a rate of 100 mA g^{-1}, 1111 mA

h g^{-1} at 300 mA g^{-1}, and 645 mA h g^{-1} at 1000 mA g^{-1}, and maintaining a reversible capacity of 445 mAh g^{-1} even at a high current density of 2000 mA g^{-1}. Moreover, when the current density is reversed back to the initial low current rate at 100 mA g^{-1}, the reversible capacity of the cell is recovered to the original value, that is 1273 mA g^{-1}, and it remains stable over the next ten cycles. This implies that the nanoflake-like architectures are robust enough to tolerate severe volume changes during the rate capability studies at varying current densities, which is a characteristic that is of considerable interest for high power applications. The CV curves of the electrode scanned at 3 mV s^{-1} are shown in Fig. 4d. In these curves, the main redox couple peaks observed at 2.08 (anodic) and 0.86 V (cathodic) in the first cycle are attributed to the reversible reactions of Li-ions with Co_3O_4 (reduction of Co_3O_4 to Co and the oxidation of Co to Co^{n+}) [7, 33]. The overlapping of the CV curves in the second cycle indicates the favorable stability of the nanoflakes. Further, the CV curves with a wide integral area suggest the expected contribution from the electrode–electrolyte interface through the capacitive behavior that is useful for the extra capacity gained from the porous ultra-thin flakes of Co_3O_4 with a large surface area; this phenomenon is apparently reported for a variety of metal oxide nanostructures [34–36]. To clarify the structural morphology of the porous Co_3O_4 nanoflakes after cycling, we carried out TEM analysis of the electrode that was collected after ten consecutive cycles. As shown in the inset image of Fig. 4d, the porous nanoflake shape is preserved (marked by circles); the other part of the image shows the presence of aggregated amorphous flakes together with the final side products such as Li_2O and the SEI film, indicating that a major portion of the nanoflake-like architectures can sustain long-term cycling.

4. CONCLUSION

In summary, we developed a simple room-temperature approach for the synthesis of disorderly arranged hierarchical arrays of Co_3O_4 nanoflakes. Compared to other state-of-art methods in non-aqueous media, our method is original and successfully produced Co_3O_4 nanostructures at room temperature. SEM and TEM analysis revealed nanostructures composed of mesoporous flakes with ultra-thin walls predominantly exposing the (111) crystal planes. When evaluated as an electrode material in lithium-ion cells, the Co_3O_4 nanoflake sample showed an exceptional anode performance with a high capacity, excellent cycle life, and high rate capability. This superior performance is ascribed to the mesoporous nanoflake-like morphology together with the predominantly exposed reactive (111) facets. Our room-temperature approach represents an experimental framework that can be extended to other metal oxides, thus paving a new facile route to the synthesis of novel materials.

AUTHOR CONTRIBUTIONS
Keun Yong Sohn and Venugopal Nulu drafted the manuscript. Venugopal Nulu designed the experiments, prepared all the samples, and characterized them. Arunakumari Nulu performed electrochemical testing and analyzed the results.

CONFLICTS OF INTEREST
The authors declare no conflict of interest.

References

1. C. N. R. Rao, *Annu. Rev. Phys. Chem.*, 40 (1989) 326.
2. A. S. Arico, P. Bruce, B. Scrosati, J. M. Tarascon, W. Schalkwijk, *Nat. Mater.*, 4 (2005) 377.
3. J. Lee, M. C. Orilall, S. C. Warren, M. Kamperman, F. J. Disalvo, U. Wiesner, *Nat. Mater.*, 7 (2008) 222.
4. J. Chakhalian, J. W. Freeland, G. Srajer, J. Strempfer, G. Khaliullin, J. C. Cezar, T. Charlton, R. Dalgliesh, C. Bernhard, G. Cristiani, H.-U. Habermeier, B. Keimer, *Nat. Phys.*, 2 (2006) 244.
5. C. M. Ban, Z. C. Wu, D. T. Gillaspie, L. Chen, Y. F. Yan, J. L. Blackburn, A. C. Dillon, *Adv. Mater.*, 22 (2010) E145.
6. J. Chen, L. N. Xu, W. Y. Li, X. L. Gou, *Adv. Mater.*, 17 (2005) 582.
7. P. Poizot, S. Laruelle, S. Grugeon, L. Dupont, J. M. Tarascon, *Nature,* 407 (2000) 496.
8. Z. S. Wu, W. C. Ren, L. Wen, L. B. Gao, J. P. Zhao, Z. P. Chen, G. M. Zhou, F. Li, H. M. Cheng, *ACS Nano,* 4 (2010) 3187.
9. K. F. Zhong, X. Xia, B. Zhang, H. Li, Z. X. Wang, L. Q. Chen, *J. Power Sources,* 195 (2010) 3300.
10. N. Du, H. Zhang, B. Chen, J. B. Wu, X. Y. Ma, Z. H. Liu, Y. Q. Zhang, D. Yang, X. H. Huang, J. P. Tu, *Adv.Mater.*, 19 (2007) 4505.
11. X. W. Lou, D. Deng, J. Y. Lee, J. Feng, L. A. Archer, *Adv. Mater.*, 20 (2008) 258.
12. W. A. V. Schalkwijk, B. Scrosati, Advances in lithium-ion batteries. Kluwer Academic/ Plenum Publishers NY, (2002).
13. C. J. Jaftaa, F. Nkosi, L. Le Roux, M. K. Mathea, M. Kebedea, K. Makgop, Y. Song, D. Tong, M. Oyama, N. Manyala, S. Chend, K. I. Ozoemena, *Electrochim. Acta,* 110 (2013) 228; (b) H. Pang, F. Gao, Q. Chen, R. Liu, Q. Lu, *Dalton Trans.,* 41 (2012) 5862.
14. L. Cui, J. Li, X. Zhang, *J. Appl. Electrochem.,* 39 (2009) 1871.
15. L. Wang, X. Liu, X. Wang, X. Yang, L. Lu, *J. Mater. Sci.,* 22 (2011) 601.
16. A. Rumplecker, F. Kleitz, E.L. Salabas, F. Schüth, *Chem. Mater.*, 19 (2007) 485.
17. Y. Xuan, R. Liu, Y.Q. Jia, *Mater. Chem. Phys.,* 53 (1998) 256.
18. M. Hamdani, J.F. Koenig, P. Chartier, *J. Appl. Electrochem.*, 18 (1988) 568.
19. M.E. Baydi, G. Poillerat, J.L. Rehspringer, J.L. Gautier, J.F. Koenig, P. Chartier, *J. Solid State Chem.,* 109 (1994) 281.
20. Y. I. Jang, H. F. Wang, Y. M. Chiang, *J. Mater. Chem.* 8 (1998) 2761.
21. G. Furlanetto, L. Formaro, *J. Colloid Interface Sci.*, 170 (1995) 169.
22. H. Y. Liang, J. M. Raitano, L. H. Zhang, S. W. Chan, *Chem. Commun.* 48 (2009) 7569.
23. D. Zou, C. Xu, H. Luo, L. Wang, T. Ying, *Mat. Lett.*, 62 (2008) 1976.
24. N. Venugopal, D.-J. Lee, Y. J. Lee, Y.-K. Sun, *J. Mater. Chem. A,* 1 (2013), 13164.
25. J. Feng, H. C. Zeng, *Chem. Mater.,* 15 (2003) 2829.
26. H.C. Zenga, Y.Y. Lim, *J. Mater. Res.*, 15 (2000) 1250.
27. OA. Fouad, SA. Makhlouf, GAM. Ali, AY. El–Sayed, *Mater Chem Phys.*, 128 (2011) 70.
28. (a) Y. Shan, L. Gao, *Mat. Chem. Phy.*, 103 (**2007)** 206. (b) B. J. Li, H.Q. Cao, J. Shao,; G.Q. Li, M. Z. Qu, G. Yin, *Inorg. Chem.*, 50 (2011) 1628.
29. B. G. Choi, S. J. Chang, Y. B. Lee, J. S. Bae, H. J. Kim, Y. S. Huh, *Nanoscale* 4 (2012) 5924.
30. Z. Zhang, L. Li, Q. Xu, B. Cao, *RSC Adv.*, 5 (2015) 61631.
31. L. Hu, N. Yan, Q. W. Chen, P. Zhang, H. Zhong, X. R. Zheng, Y. Li, X.Y. Hu, *Chem. Eur. J.*, 18 (2012) 8971.
32. O. M. Yaghi, H. L. Li, T. L. Groy, *J. Am. Chem. Soc.*, 118 (1996) 9096-9101.

33. D. Barreca, M. Cruz-Yusta, A. Gasparotto, C. Maccato, J. Morales, A. Pozza, C. Sada, L. Sánchez, E. Tondello, *J. Phys. Chem. C,* 114 (2010) 10054.
34. X. M. Liu, Z. D. Huang, S. W. Oh, B. Zhang, P. C. Ma, M. M. F. Yuen, J. K. Kim, *Composites Sci. Tech.*, 72 (2012) 121.
35. Y. Zhang, X. Z. Zhang, H. L. Zhang, Z. G. Zhao, F. Li, C. Liu, H. M. Cheng, *Electrochim. Acta,* 51 (2006) 4994.
36. Y. M. Lin, P. R. Abel, D. W. Flaherty, J. Wu, K. J. Stevenson, A. Heller, C. B. Mullins, *J. Phys. Chem. C.*, 115 (2011) 2585.